Article

Precursor-Mediated Linear- and Branched-Polytypism Control in $Cu_\alpha Zn_\beta Sn_\gamma Se_\delta$ Colloidal Nanocrystals Using a Dual-Injection Method

Huan Ren, Zhe Li, Yuanwei Sun, Peng Gao, Conor McCarthy, Ning Liu, Hongxing Xu, and Kevin M. Ryan*

ACCESS | 📊 Metrics & More | 📄 Article Recommendations | 🆂🅸 Supporting Information

ABSTRACT: Control of polytypism in colloidal nanocrystals allows for a shape evolution from 0D to 3D and also provides an opportunity to tailor physical properties that are crystal phase dependent. Initiating polytypism in nanostructures is a function of multiple different control parameters that dictate nucleation and growth, including reaction temperature, ligands, and precursors. This is further complicated as the number of metal ions increases in progressing from binary to ternary to quaternary compositions. Here, a synthesis method with dual injections is developed to initiate two- and three-dimensional polytypism in the nonstoichiometric$\alpha\beta\delta$ $Cu_\alpha Zn_\beta Sn_\gamma Se_\delta$ system simply by changing a single commercially available chemical precursor. Synthesis parameters were developed to grow single-crystal wurtzite and zinc-blende forms with a further extension to linear and branched morphologies deriving from nucleation in one phase and growth termination in the other. Photoluminescence measurements were carried out on the particles at a low temperature with emission peaks ranging from ~1.93 to ~2.32 eV observed.

I. INTRODUCTION

Colloidal semiconductor nanocrystals (NCs) have attracted significant attention for their unique properties that can be synthetically engineered by size, morphology, composition, and surface energy state tuning.[1−4] These size-dependent electronic and optical properties grant these "artificial atoms" vast potential in photovoltaics, catalysis, lighting/displays, energy storage, thermoelectrics, sensors, and bioimaging applications.[5,6] Copper-based colloidal semiconductor NCs, such as copper indium sulfide (CIS), copper indium gallium sulfide, (CIGS), and their analogues,[7−9] have attracted attention as more sustainable and less toxic alternatives to cadmium and lead-containing materials. The successful colloidal syntheses of Cu_2ZnSnS_4 (CZTS),[10−12] $Cu_2ZnSnSe_4$ (CZTSe),[13,14] and $Cu_2ZnSn(S_{1−x}Se_x)_4$ (CZTSSe)[3,15] nanocrystals have demonstrated the versatility in controlling the crystal phase, composition, and morphology of these multi-component nanomaterials. Furthermore, they also have a relatively low energy requirement for defects and abundant stoichiometric/nonstoichiometric crystal phases that provide a wide application window across electronic and optoelectronic systems.[3,15−19] CZTSSe NCs synthesized using a solution-based method have already demonstrated promising potential for photovoltaics with conversion efficiencies of 12.6%.[20−22] CZTSe NCs are an ideal PV material with a suitable and direct band gap of (1.0−1.5 eV)[23−25] and intrinsic p-type conductivity with a high absorption coefficient of 10^5 cm$^{−1}$.[26,27] Other related studies have also reported their strong thermoelectric properties that are strongly crystal phase dependent.[28,29]

The hot injection colloidal approach has persisted in the past decade as the most common approach for CZTSe NC synthesis due to their versatility and fine control over nanoparticle uniformity.[1,30,31] The separation of anionic and cationic precursors by injection provides a high level of control in nucleation and growth for complicated systems involving multiple precursors.[32−37] Typically, hexagonal wurtzite (WZ) phase CZTSe NCs have been formed using metal-oleate and diphenyl diselenide as precursors with a moderate temperature of around 250 °C and are generally nonstoichiometric.[19,38,39] On the other hand, the incorporation of oleylamine (OLAM) and trioctylphosphine oxide (TOPO) ligands led to the formation of Kesterite CZTSe NCs.[40] Compositional variation in CZTSe NCs was further tuned using various phosphonic acids to adjust the reactivity of Zn monomers.[13] Other researchers focused on the synthesis of stannite or kesterite CZTSe NCs mainly employing Se powder as the anionic precursor source at a relatively high temperature (280−300 °C).[29,41−43]

Polytypism can be defined as the occurrence of two different crystal phases in the same crystalline entity.[44] In I−IV−VI and I−II−IV−VI systems, hexagonal wurtzite (WZ) and cubic zincblende (ZB) are the most common polymorphs, where either linear or branched polytypism can occur on WZ(0002) and ZB⟨111⟩ facets due to their similar atomic arrangement and small energy difference.[45,46] As the most representative structure in branched polytypism, tetrapod nanocrystals nucleate with a ZB core with 4 equiv -ZB⟨111⟩ facets, on which the WZ(0002) facets of four WZ arms are tetrahedrally attached.[47] This tetrapod structure was previously observed in the binary systems such as CdSe,[48−50] CdTe,[47,49,50] CdS,[51−54] ZnSe,[55] and ZnTe[56] NCs. More recently, some developments have been made in branched polytypism in the multielemental system. In a study on $Cu_2Cd_xSnSe_y$ (CCTSe) tetrapod NCs,[57] for example, the initial ZB core undergoes twinning to form a pentatetrahedral ZB core with the four WZ arms finally growing from the secondary ZB core to form tetrapods. In the ternary tetrapod NC system (Cu_2SnSe_3 (CTSe)), diphenyl diselenide (DPhDSe) was used as the Se source allowing the crystal growth to switch from the thermodynamically stable ZB to the dynamically stable WZ phase, providing that a suitable temperature drop exists before and after the hot injection.[58] The branching also allows for the assembly of the super-structures, which can provide ordered 3D network structures suitable for device fabrication.[59−61] It was also observed in hybrid NC polymer photovoltaic devices that the high-electron affinity of the heterostructure provides a better electron percolation pathway for better device performance.[62−64] Some studies also demonstrated that these polytypic interfaces can improve the thermoelectric performance significantly.[65−67]

Another common type of polytypic structure is known as the linear polytype, which nucleates in the WZ phase with a subsequent switch to ZB phase growth on either the more reactive -WZ(0002) facet resulting in the arrow-shaped NCs or both ±WZ(0002) facets to form ellipsoidal NCs. A series of $Cu_2CdSn(S_{1−x}Se_x)_4$ (CCTSSe) polytypic nanocrystals were reported, where increasing the Cd content allowed control of polytypism either to form one or two cubic terminations.[68] When it comes to polytypism in the Cu_2ZnSnS_4 (CZTS) system, the formation of acorn-shaped NCs from single-sided polytypic growth on single-phase ellipsoidal NCs were also reported. Moreover, when the reactivity of the Zn precursor was reduced, pencil-shaped NCs grew due to single-sided polytypic growth.[10] In an another shape control study on $Cu_2ZnSn(SSe)_4$ (CZTSSe), it was suggested that when the reactivity of the Cu precursor was increased, double-sided polytypism was less favored compared to single-sided.[15]

Interestingly to date, all reports of polytypism in copper−tin−zinc−chalcogenides have necessitated the presence of sulfur with no reports to date in CZTSe polytypes. This composition is very interesting from an application perspective with the optimal band gap and absorption coefficients for photovoltaics. There are additional challenges to date that have manifested in the colloidal synthesis of CZTSe NCs where there is a requirement for metal-oleate as precursors, which are not commercially available and require further processing from sodium oleate in addition to issues with the Zn-poor nature of the particles.[29,38,42,69] Herein, we report our studies on linear and branched polytypism in the CZTSe system using only commercially available chemicals, taking precursor selection and temperature as the control factors.

II. EXPERIMENTAL SECTION

II.I. Materials. Copper(II) acetylacetonate ($Cu(II)(acac)_2$; >99.99%), copper(I)chloride (Cu(I)Cl>97%), tin(IV) acetate (Sn-$(Ac)_4$, >99.99%), tin(II)chloride ($SnCl_2$, >97%), zinc acetate ($Zn(Ac)_2$, >99.99%), zinc chloride ($ZnCl_2$, >99.99%), 1-dodeca-nethiol (1-DDT, 98%), diphenyl diselenide (DPhDSe, 98%), and oleylamine (OLA, technical grade, 70%) were purchased from Sigma-Aldrich. All chemicals were used as purchased without further processing.

II.II. Synthesis of WZ CZTSe NCs (Hexagonal Plates). In a typical synthesis, $Cu(II)(acac)_2$ (0.5 mmol) and OLAM (10 mL) were added in a three-neck flask and evacuated at 60 °C for 20 min. The solution was then heated to 250 °C in 15 min under the protection of argon. Two injection solutions were injected during the above-stated temperature range (60−250 °C). Injection 1 consists of DPhDSe (0.625 mmol), Sn(II)(Ac)$_2$ (0.25 mmol), and OLAM (2.5 mL) and was injected at 155 °C, while injection 2 contains $Zn(Ac)_2$ (0.25 mmol) and OLAM (1.5 mL) and was injected 40 s after Injection 1. After the mother solution temperature reached 250 °C, the reaction was allowed to proceed at this temperature for another 15 min with continuous stirring with a magnetic stirrer. The reaction was terminated by removing the heating mantle and quenched with 30 mL of toluene when the temperature was cooled to 90 °C naturally. The product was washed two times with toluene/isopropanol (3:1) at 4000 rpm for 2 min.

II.III. Synthesis of Linear-Polytypic CZTSe NCs (Ellipsoids). $Cu(II)(acac)_2$ (1 mmol) and OLAM (10 mL) were added to a three-neck flask and evacuated at 60 °C for 20 min. The solution was then heated to 250 °C in 15 min under the protection of argon. Two injection solutions were injected during the above-stated temperature range, 60−250 °C. Injection 1 contains DPhDSe (1.25 mmol), Sn(II)Cl$_2$ (0.5 mmol), and OLAM (2.5 mL). Injection 2 contains $Zn(Ac)_2$ (0.5 mmol) and OLAM (1.5 mL). Injection 1 was injected into the Cu/OLAM mixture at 155 °C via a syringe followed by Injection 2, 40 s after the first injection. After the solution temperature reached 250 °C, the reaction was allowed to proceed at this temperature for another 15 min with continuous stirring using a magnetic stirrer. The reaction was terminated by removing the heating mantle and quenched with 30 mL of toluene when the temperature was cooled to 90 °C naturally. The product was washed two times with toluene/isopropanol (3:1) at 4000 rpm for 2 min.

II.IV. Synthesis of ZB CZTSe NCs (Pyramidal Tetrahedrons). In a typical synthesis, Cu(I)Cl (0.25 mmol), $Zn(Ac)_2$ (0.125 mmol), Sn(IV)Ac$_4$ (0.125 mmol), and OLAM (10 mL) were added in a three-neck flask and evacuated at 60 °C for 20 min. The solution was then heated to 310 °C in 20 min under the protection of argon. The injection solution contains Se powder (0.5 mmol), 120 μL 1-DDT, and OLAM (1 mL) (Se/1-DDT = 1:1, molecular ratio). The injection solution was then injected into the flask at 310 °C after which the reaction proceeded for another 20 min at this temperature after the injection. The reaction was stopped by removing the heating mantle and cooled naturally to 90 °C, then quenched with 30 mL of toluene. The product was washed two times with toluene/isopropanol (3:1) at 4000 rpm for 2 min.

II.V. Synthesis of Branched-Polytypic CZTSe NCs (Tetrapods). Cu(I)Cl (0.25 mmol) and OLAM (10 mL) were added in a three-neck flask and evacuated at 60 °C for 20 min. The mother solution was heated to 310 °C in 20 min under argon protection. Injection solution 1 contains DPhDSe (0.3 mmol), Sn(IV)Ac$_4$ (0.125 mmol), and OLAM (2.5 mL). Injection solution 2 contains $Zn(Ac)_2$ (0.125 mmol) and OLAM (1.5 mL). Injection solution 1 was injected into the flask at 310 °C, and Injection solution 2 was injected 7 s after Injection 1. The solution was allowed to proceed at the same temperature for 15 min after the two injections. The reaction was stopped by removing the heating mantle and cooled naturally to 90 °C, then quenched with 30 mL of toluene. The product was washed two times with toluene/isopropanol (3:1) at 4000 rpm for 2 min.

III. RESULTS AND DISCUSSION

III.I. Wurtzite CZTSe Nanocrystals. The as-synthesized wurtzite CZTSe NCs have a quasi-hexagonal plate shape with an average diameter of 17.35 nm (Figure 1a). In Figure 1b, the
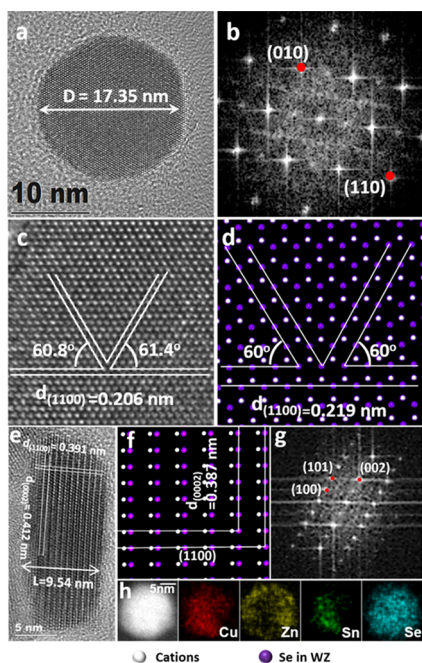
Figure 1. (a) HRTEM image of a WZ hexagonal $Cu_\alpha Zn_\beta Sn_\gamma Se_\delta$ (CZTSe) nanoplate from zone axis WZ[0002]. (b) Corresponding FFT of *a*. (c) Magnified HRTEM of *a* with the atomic arrangement on WZ[0002] facet exposed. (d) Corresponding atomic arrangement model with cations in white and Se in purple. (e) HRTEM image of a WZ hexagonal CZTSe nanoplate viewed from the side. (f) Corresponding atomic arrangement model with cations in white and Se in purple. (g) FFT from the lateral facet of a hexagonal CZTSe nanoplate. (h) STEM image of a WZ CZTSe plate NC with corresponding STEM-EDX elemental maps related to Cu (red), Zn (yellow), Sn (green), and Se (cyan).

fast Fourier transform (FFT) from the WZ [0002] direction is used to confirm the crystallinity of the structure and calculate the *d*-spacings. The three equivalent (1100) facets have a *d*-spacing of ~0.21 nm and form ~60° angles with one another (Figure 1c), which is in good agreement with the atomic modelling in Figure 1d. High-resolution transmission electron microscopy (HRTEM) in Figure 1e allows further analysis of the CZTSe WZ crystal structure in a nanoplate on its edge (thickness of ~9.5 nm). The characteristic ABABA... packing along the *c*-axis (WZ(0002)) allows the direct measurement of the *d*-spacing, ~0.39 nm, which is in good agreement with the atomic modelling in Figure 1f. The FFT in Figure 1g confirms the crystalline structure in the sample and highlights the layered atomic structure with the diffraction dots. The *d*-spacings of planes (100), (101), and (002) are indexed in the FFT (~0.32, ~0.29, ~0.33 nm). The elemental maps from the energy-dispersive X-ray spectroscopy in the scanning transmission electron microscope (EDX-STEM) confirm the presence of four elements within the nanostructure (Figure 1h). The diameter and thickness of the WZ NCs can be tuned by changing the Zn/Sn addition ratio (Supporting Information: HRTEM images and EDX spectra, Figures S1 and S2, respectively).

III.II. CZTSe Linear Polytypes. A typical synthesis for the linear-polytypic structure is carried out at the same temperature and solvent as hexagonal WZ nanoplate synthesis with the only change being the use of $Sn(II)Cl_2$ instead of $Sn(II)(Ac)_2$. Figure 2a shows a typical linear-polytypic
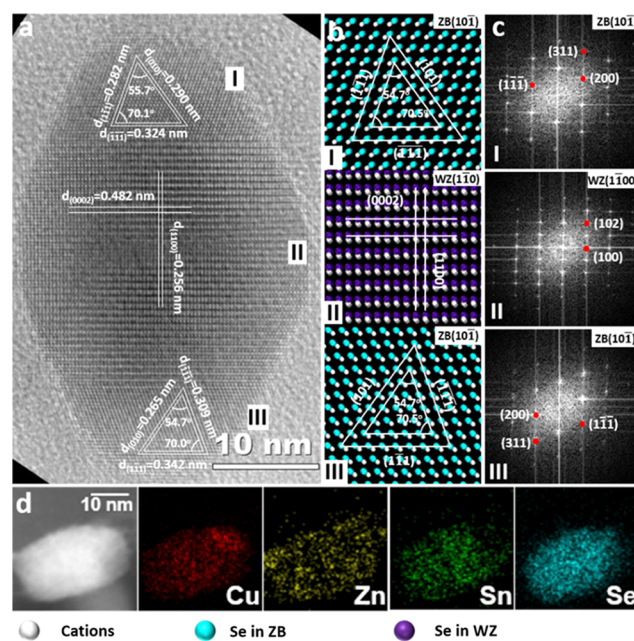
Figure 2. (a) HRTEM image of an ellipsoidal CZTSe NC with *d*-spacings indexed in three polytypic areas I, II, III, with the corresponding atomic arrangement models in (b) and FFT in (c). (d) STEM image of a single-ellipsoidal CZTSe NC with corresponding STEM-EDX elemental maps related to Cu (red), Zn (yellow), Sn (green), and Se (cyan).

CZTSe NC (~41 nm in length and ~27 nm in diameter) that has a ZB−WZ−ZB arrangement. This structure started its growth from the WZ phase along its *c*-axis and subsequently switched its growth to the ZB phase on both WZ ends. The ZB−WZ interphases, namely, the top polytypic interphase, WZ(000$\bar{2}$) and ZB($\bar{1}\bar{1}\bar{1}$), and the bottom polytypic interphase, WZ(0002) and ZB(1$\bar{1}$1), are presented and indexed in the HRTEM image.

Based on the HRTEM in Figure 2a, and underpinned by the established theory that the inversive polarity is not energetically favorable,[57,70,71] a corresponding atomic model of the linear polytype is built in Figure 2b. It is demonstrated that the top WZ phase facet, WZ(000$\bar{2}$), is negatively charged from the exposed Se anions with the attached ZB($\bar{1}\bar{1}\bar{1}$) being positively charged. On the contrary, the bottom WZ phase has a positively charged facet, WZ(0002) with unbounded cations, while the attached ZB phase facet, ZB(1$\bar{1}$1), is negatively charged. FFT of three polytypic areas is used to analyze the crystal phase and calculate the *d*-spacings of respective sections in Figure 2c. The *d*-spacings of planes (111), (311), and (200) are indexed in the top ZB phase (~0.33, ~0.17, ~0.269 nm). The *d*-spacings of planes (102) and (100) are indexed in the middle WZ phase (~0.16, ~0.23 nm). The *d*-spacings of planes (111), (311), and (200) are indexed in the bottom ZB phase (~0.32, ~0.16, ~0.269 nm). EDX maps in Figure 2d confirm the presence of all four elements.

Comparing WZ and linear polytypic synthesis conditions, only the middle-stage Sn precursor is changed. In the

formation of WZ NCs, the less reactive $Sn(II)(Ac)_2$ with lower growth rate[72] is used to promote the growth in the peripheral directions (e.g., $[0\bar{1}00]$ and $[1\bar{1}00]$), resulting in the hexagonal plate shape. In contrast, the more reactive $Sn(II)Cl_2$ was used for the growth stage of the linear polytype after nucleation, where the elongation along the initial WZ phase c-axis ($[0002]$) is preferred at first. When it comes to the sole Sn precursor difference triggering the occurrence of linear polytypism, according to previous studies, metal acetates and metal acetylacetonates form coordination complexes with oleylamine,[73−75] such as $[Sn(OLAM)_4]^{2+}(acac^-)_2$. The six-member chelate tightly bonded to the center metal atom provides steric hindrance that should favor the continuous growth of the less densely packed WZ phase.[45] As for the occurrence of linear polytypism, the Sn chlorides form chloride complexes with oleylamine,[76−78] where the strongly nucleophilic chloride complexes favor the positively charged facets, resulting in the growth of the ZB phase which has more positively charged facets (e.g., ZB(111), ZB(001)) than WZ.

III.III. Zinc-Blende CZTSe. The optimal synthesis to nucleate ZB NCs required switching to copper chloride (as opposed to acetate) in addition to a much higher injection temperature (310 °C) with a small drop to the growth temperature (300 °C) in contrast to a lower injection temperature and ramp to growth for WZ. 1-DDT is used in ZB synthesis primarily to aid the dissolution of the Se powder in oleylamine. Our observations show that the presence of 1-DDT does not influence the morphology or size distribution of the as-synthesized NCs (Supporting Information: low-magnification TEM image and size distribution analysis, Figure S5).

As shown in the high-angle annular dark field of scanning transmission electron microscopy (HAADF-STEM) image in Figure 3a, a typical ZB NC is ~20 nm in diameter with the characteristic atomic arrangement of the ZB phase. From zone-axis orientation $ZB[10\bar{1}]$, the interphases of crystal twinning are clearly observed (red lines) in Figure 3b. The ZB−ZB twinning occurs along the crystal growth direction, $ZB[\bar{1}\bar{1}\bar{1}]$ (white line), and mirroring at $ZB(11\bar{1})$ planes. The twinning mirror plane and crystal growth direction form an angle of 70.5°, as shown in Figure 3c. The corresponding atomic model displays the same oriented mirror structure in the same color. The same NC was oriented to align with zone-axis direction $ZB[11\bar{2}]$ in Figure 3d. In the magnified area of interest (Figure 3e), the lattice of crystal growth direction, $ZB[11\bar{1}]$, can be clearly observed. Orientating the 3D atomic model to the matching facet of the HAADF image (Figure 3f), we can observe that although mirror structures have different orientations, their projections look identical and the twinning interphases are not discernable from the $ZB[11\bar{2}]$ direction. STEM elemental mappings of a single ZB NC in Figure 3g show the presence and homogeneous distribution of elements Cu, Zn, Sn, and Se. In our observation, most of the ZB NCs are rich in twinning stacking faults that can be attributed to the relatively slow growth rate induced by OLAM-Se.[79,80]

III.IV. Branched Polytype CZTSe. The synthesis of branched polytypes, different from linear polytypes, starts from the growth of the ZB phase with key synthetic differences being the use of copper chloride as the copper precursor at a higher temperature.

In Figure 4a, the TEM image of a single CZTSe tetrapod NC is taken from orientation $ZB[11\bar{1}]/WZ[0002]$ with one arm pointing upwards. The crystal phase contrast outlines the
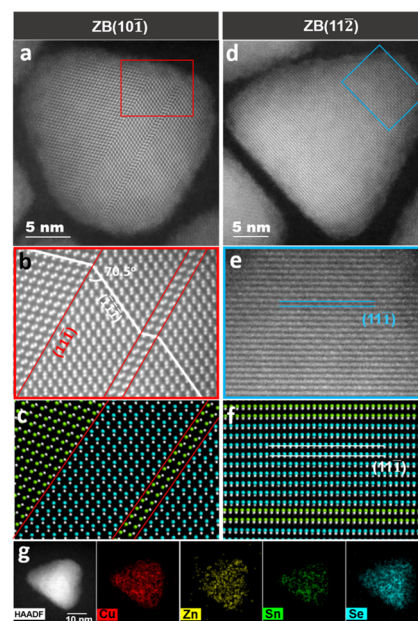
Figure 3. (a) HAADF of a quasi-tetrahedron ZB CZTSe nanocrystal from zone-axis direction, $ZB[10\bar{1}]$. (b) Magnified area from (a) with crystal twinning stacking faults marked red lines and crystal growth direction indicated by white lines. (c) Corresponding atomic modelling of (b) with different mirror structures colored differently. (d) HAADF of a quasi-tetrahedron ZB CZTSe NC from zone-axis direction, $ZB[11\bar{2}]$. (e) Magnified area from (d). (f) Corresponding atomic modelling of (e) with different mirror structures. (g) STEM image of a quasi-tetrahedron ZB CZTSe NC with corresponding STEM-EDX elemental maps related to Cu (red), Zn (yellow) Sn (green), and Se (cyan).
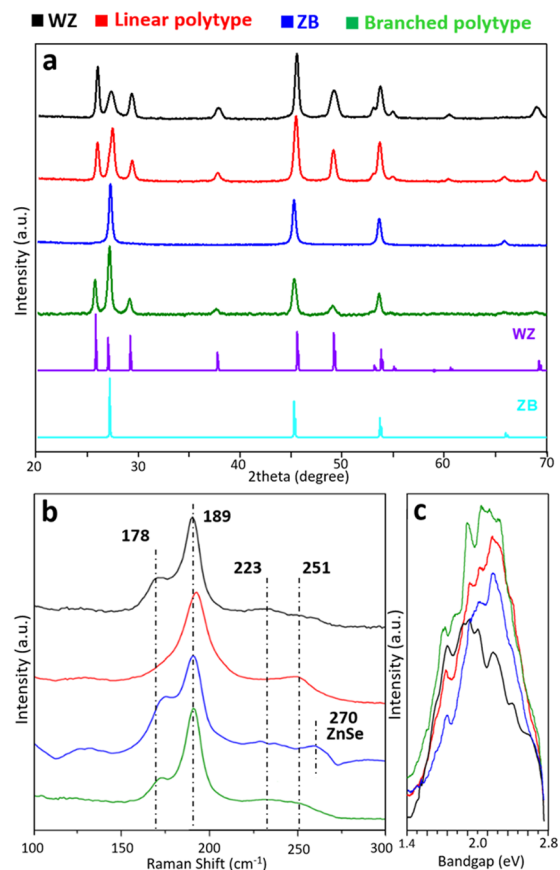
quasi-tetrahedron core (area IV) with I, II, III the WZ arms. FFT analysis, Figure 4b, allows the calculation of the d-spacing of facet (102) in the WZ phase at ~0.256 nm and the d-spacings of facet (220) and (111) in the ZB phase, respectively. The three WZ arms are tetrahedrally attached to the ZB core at interphases $ZB(11\bar{1})$ and $WZ(0002)$. The three interphases intercept with the viewing plane ZB (111) to form an almost perfect regular triangle. HAADF-STEM is employed to further analyze the polytypic interphases from the same orientation as Figure 4a. Figure 4c focuses on the outer WZ arm in which the c-axis aligns with the TEM incident beam. The characteristic hexagonal patterns are clearly displayed in Figure 4e with commonly observed planes indexed in the HAADF image as well as the matching atomic model. The area of interest in the tetrapod arm (Figure 4g) shows the slight off-plane facet $WZ(1\bar{1}00)$ due to the nonplanar orientation of the arm in the morphological arrangement. Compared to the corresponding atomic model, the lattices of $WZ(2\bar{2}00)$ can be seen in the HAADF image while $WZ(0002)$ cannot be observed. To study the ZB interphase, the sample tetrapod NC was turned to have the fourth arm pointing away from view in Figure 4d while the zone-axis orientation remains the same as Figure 4c. The only difference between the atomic arrangement in the two crystal phases is the middle atomic site in the six-member atomic unit where the WZ has a vacant atomic site while the ZB has an occupied atomic site, as shown in Figure 4f. This resemblance allows the growth transmission from the ZB to the WZ phase. In Figure 4h, the STEM elemental mappings of tetrapod NCs
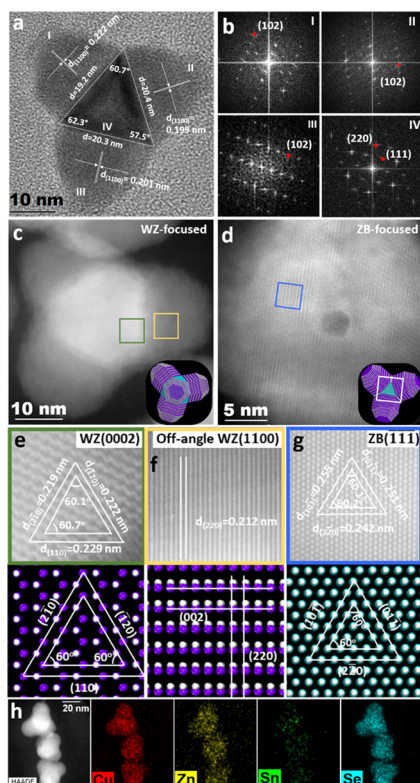
Figure 4. (a) TEM image of a single CZTSe tetrapod NC from direction WZ[0002]/ZB[11$\bar{1}$]. (b) Corresponding FFT of areas I, II, III, and IV in (a). (c) HAADF image of a single CZTSe tetrapod NC from direction WZ[0002]/ZB[111] focusing on the WZ (0002) facet with bottom inset of a structural model. (d) HAADF image of a single CZTSe tetrapod NC from direction WZ[0002]/ZB[111] focusing on the ZB (111) facet with bottom inset of a structural model. (e) Area of interest in the core of (c) with the matching atomic model. (f) Area of interest in the arm of (c) with the matching atomic model. (g) Area of interest in (d) with the matching atomic model. (h) STEM image of three CZTSe tetrapod NCs with corresponding STEM-EDX elemental maps related to Cu (red), Zn (yellow), Sn (green), and Se (cyan).

Figure 5. (a) XRD spectra of as-synthesized CZTSe hexagonal WZ NCs (black), CZTSe ellipsoidal NCs (red), CZTSe quasi-tetrahedron ZB NCs (navy), and CZTSe tetrapod NCs (olive). (b) Raman spectra of as-synthesized CZTSe hexagonal WZ NCs (black), CZTSe ellipsoidal NCs (red), CZTSe quasi-tetrahedron ZB NCs (navy), and CZTSe tetrapod NCs (olive). (c) Low-temperature photoluminescence (70K) band gap energy spectra of CZTSe hexagonal WZ NCs, CZTSe ellipsoidal NCs, CZTSe pyramidal ZB NCs, and CZTSe tetrapod NCs.

show the presence and homogeneous distribution of elements Cu, Zn, Sn, and Se.

In Figure 5a, the XRD results of each sample are consistent with HRTEM crystal phase observations. The lattice parameters were calculated from the experimental XRD pattern by fitting the main diffraction peaks corresponding to the cubic and wurtzite structures. The lattice parameters of WZ are $a = b = 4.1$ Å and $c = 6.8$ Å calculated from the fitting of (002) and (110) planes. The lattice parameter calculated for the cubic structure is $a = b = c = 5.8$ Å, calculated from the fitting of the (111) plane. The hexagonal WZ plate NCs have an XRD pattern that is consistent with the WZ reference pattern with major peaks listed in Table S1. The ellipsoidal NCs have a mixture of both WZ and ZB crystal phases with respective percentages of 77.3 and 22.7%, with major peaks and Rietveld refinement in Supporting Information: Table S2 and Figure S3, respectively. The Quasi-tetrahedron NCs' pattern agrees with the ZB crystal reference, with major peaks listed in Table S3. The branched-polytypic NCs have a mixture of both WZ and ZB crystal phases with respective percentages of 45 and 55%. Major peaks and Rietveld refinement are included in the Supporting Information: Table S4 and Figure S4, respectively. The Raman spectroscopy was used to
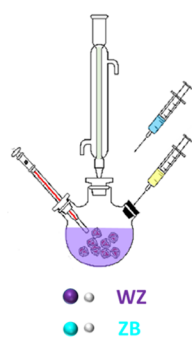
eliminate the possibility of the presence of binary and ternary impurities that remain undetected in XRD. As shown in Figure 5b, a typical Raman spectrum of CZTSe has four signature peaks, 178, 189, 223, and 251 cm^{-1}, All four signature peaks are in good agreement with previous research.[81,82] There is no indications of binary impurity presence such as Cu$_x$Se[83] (260 cm^{-1}), SnSe$_2$ and SnSe[84,85] (110, 150 cm^{-1}), ZnSe[86] (270 cm^{-1}) in WZ, linear and branched polytypes. The peak at 270 cm^{-1} in the ZB spectrum indicates the possibility of a small amount of ZnSe binary composition. In addition, all four samples are also free from possible ternary impurity, CTSe[87] (180 cm^{-1}).

To understand the band structures of CZTSe NCs, low-temperature (77 K) photoluminescence (PL) experiments were carried out with a 405 nm laser diode (Thorlabs CPS405), with results shown in Figure 5c. No PL signal was observed at room temperature, suggesting that these CZTSe NCs have very low quantum efficiencies at room temperature. When the temperature decreases to 77 K, all samples have multiple emission peaks, indicating a complicated band structure. The strongest emission peak of the WZ NCs is centered around ~1.95 eV, while the strongest emission peak of the ZB NCs has a higher energy at ~2.34 eV. The peak

Table 1. Synthesis Condition Details for Four Types of NCs

	Shape	Phase	Chemicals in flask	1st injection	2nd injection	Injection temp	Growth temp	Chemical composition %
Low temperature		WZ	Cu(II)(acac)$_2$ oleylamine	Sn(II)(Ac)$_2$ DphDSe	Zn(Ac)$_2$	155°C	250°C	Cu 28.37 Zn 9.60 Sn 12.84 Se 49.19
Low temperature		Linear polytypic	Cu(II)(acac)$_2$ oleylamine	Sn(II)Cl$_2$ DphDSe	Zn(Ac)$_2$	155°C	250°C	Cu 25.84 Zn 18.20 Sn 10.69 Se 45.26
High temperature		ZB	Cu(I)Cl, Sn(IV)Ac$_4$ Zn(Ac)$_2$ oleylamine	Se powder	N/A	310°C	300°C	Cu 27.32 Zn 10.72 Sn 14.29 Se 47.63
High temperature		Branched polytypic	Cu(I)Cl oleylamine	Sn(IV)Ac$_4$ DphDSe	Zn(Ac)$_2$	310°C	300°C	Cu 33.81 Zn 9.71 Sn 15.94 Se 40.53

● ○ **WZ**
● ○ **ZB**

shape and position of two polytypic NCs match well with the combination of the WZ and ZB phases, where linear-polytypic NCs exhibit more ZB emission behavior and 3D branched-polytypic NCs have more pronounced WZ emission behavior.

The CZTSe polytypic NC synthesis is especially challenging and delicate due to the inherent complex reaction mechanisms that involve balancing the reactivity of four precursors, separation of nucleation and growth stages, and initiation of polytypism. Low-magnification dark-field images in the Supporting Information: Figure S6 illustrates that all four as-synthesized NCs have relatively high uniformity.

Table 1 outlines the key determining factors in the nucleation and growth control of each particle type. There are clear patterns with respect to precursor choice, growth temperature, and how the precursors are combined.

A key factor for the successful syntheses of WZ, linear-polytypic, and branched-polytypic structures is the inclusion of a second injection, so that the three cationic precursors are segregated as such: the Cu precursor in the flask, the Sn precursor in the first injection, and the Zn precursor in the second injection. The isolation of the Cu precursor ensures an uninterrupted nucleation between Cu and Se upon the first injection, while Sn incorporates into the system slightly later than the readily decomposed Cu precursor. At last, the Zn precursor was introduced in the 2nd injection. Therefore, each cationic precursor has its own independent incorporation window to minimize the interferences from both other cations and their thermal decomposition byproducts (Supporting Information: TEM images and size distribution histograms, Figure S7). This dual-injection method provides strong control on multiple cation incorporation balance during the nucleation and growth process when selections of precursors with different reactivities are limited. A detailed discussion can be found in the Supporting Information (Figure S8).

The four NCs can be divided into WZ-initiated structures (WZ, linear polytype) and ZB-initiated structures (ZB, branched polytype).

In the low-temperature growth (WZ and linear polytypic) shown in Table 1, the injection at 155 °C allows for pure wurtzite nucleation as the ramp progresses through the expected nucleation and growth window for WZ (220–280 °C) and remains below the ZB window (255–310 °C) ensuring nucleation phase purity. Furthermore, the relatively high WZ growth temperature eliminates the formation of large round particles and Ostwald ripening, which require a relatively low temperature (typically <180 °C).[88−91] The relatively low injection temperature (155 °C) provides a wide time frame of subsequent cationic incorporation before the

final growth temperature (250 °C). Moreover, the elevated temperature benefits cationic exchange and incorporation.

To accommodate the dual-injection approach, reactive Cu precursors such as Cu(I)Cl and Cu(acac)$_2$ are selected as the nucleation Cu precursor to ensure homogeneous burst nucleation at high nuclei concentration.[30] Equally, a highly active Zn precursor, Zn(Ac)$_2$, was used in the second injection to ensure efficient Zn incorporation.

At elevated temperatures (300 °C region), the thermodynamically stable ZB phase is favored as shown in ZB NCs and branched polytypes that both have initial growth in the ZB phase. The synthesis conditions of ZB and branched polytypes differentiate in the choice of Se precursors. In ZB NCs, it has been established that the Se powder directs crystal growth in the ZB phase regardless of the selection of cationic precursors and temperature.[19] While in branched polytypes, diorganyl dichalcogenide has previously been demonstrated to be suitable for thermodynamically favored ZB phase synthesis at higher temperatures,[92] and dynamically stable WZ growth at moderate temperatures triggered by the temperature drop before and after the dual injections.[58] Comparing the formation mechanisms, ZB NCs and branched polytype ZB cores have similar quasi-tetrahedron shape and size (diameter ∼ 20 nm). However, in all as-synthesized ZB NCs, a large amount of twinning stacking faults was observed and all branched polytype ZB cores are free from stacking faults as discussed in the previous sections. This observation indicates that ZB twinning stacking faults are favored in the presence of the Se powder, while ZB−WZ polytypism is favored when DPhDSe is used.

The chemical composition from EDX mapping indicates all four NCs have Cu-rich nonstoichiometric compositions with Sn the second-most dominant composition in the other three NCs apart from the linear polytypes, where it is superseded by Zn.

IV. CONCLUSIONS

In summary, we have developed systematic and reproducible syntheses for the formation of quaternary CZTSe nanocrystals in single-crystal (wurtzite and zinc-blende) and in polytypic (linear and branched) forms. The use of a dual-injection approach to temporally separate the cationic precursors allowed for excellent particle control, where the choice of the precursor and temperature are the key control factors in the occurrence or absence of polytypism. As CZTSe is one of the most versatile of the nanocrystal copper chalcogenides with applications in photovoltaics, thermoelectrics, and bio-labeling, the synthetic approaches developed herein will allow for a

greater toolset to tune its functional properties by crystal phase and shape.

ASSOCIATED CONTENT

Supporting Information

The Supporting Information is available free of charge at https://pubs.acs.org/doi/10.1021/acs.chemmater.0c01663.

Experimental details, TEM images, STEM images, EDX details, and XRD details (PDF)

AUTHOR INFORMATION

Corresponding Author

Kevin M. Ryan − Department of Chemical Sciences and Bernal Institute, University of Limerick, Limerick V94 T9PX, Ireland; orcid.org/0000-0003-3670-8505; Phone: +353 (61) 213167; Email: Kevin.M.Ryan@ul.ie

Authors

Huan Ren − Department of Chemical Sciences and Bernal Institute, University of Limerick, Limerick V94 T9PX, Ireland

Zhe Li − Department of Physics and Bernal Institute, University of Limerick, Limerick V94 T9PX, Ireland; School of Physics and Technology, Center for Nanoscience and Nanotechnology, and Key Laboratory of Artificial Micro- and Nano-structures of Ministry of Education, Wuhan University, Wuhan 430072, P. R. China

Yuanwei Sun − International Center for Quantum Materials and Electron Microscopy Laboratory, School of Physics, Peking University, Beijing 100871, P. R. China

Peng Gao − International Center for Quantum Materials and Electron Microscopy Laboratory, School of Physics, Peking University, Beijing 100871, P. R. China; orcid.org/0000-0003-0860-5525

Conor McCarthy − Confirm Centre & Bernal Institute, School of Engineering, University of Limerick, Limerick V94 T9PX, Ireland

Ning Liu − Department of Physics and Bernal Institute, University of Limerick, Limerick V94 T9PX, Ireland; orcid.org/0000-0003-1164-6387

Hongxing Xu − School of Physics and Technology, Center for Nanoscience and Nanotechnology, and Key Laboratory of Artificial Micro- and Nano-structures of Ministry of Education, Wuhan University, Wuhan 430072, P. R. China; orcid.org/0000-0002-1718-8834

Complete contact information is available at:
https://pubs.acs.org/10.1021/acs.chemmater.0c01663

Notes

The authors declare no competing financial interest.

ACKNOWLEDGMENTS

REFERENCES

(1) Alivisatos, A. P. Semiconductor clusters, nanocrystals, and quantum dots. *Science* 1996, 271, 933−937.

(2) Ekimov, A. I.; Onushchenko, A. A. Quantum size effect in three-dimensional microscopic semiconductor crystals. *J. Exp. Theor. Phys.. Lett.* 1981, 34, 345−349.

(3) Singh, A.; Singh, S.; Levcenko, S.; Unold, T.; Laffir, F.; Ryan, K. M. Compositionally tunable photoluminescence emission in $Cu_2ZnSn(S_{1-x}Se_x)_4$ nanocrystals. *Angew. Chem., Int. Ed.* 2013, 52, 9120−9124.

(4) Mullin, J. W. *Crystallisation*; Butterworth Heinemann: Oxford, U.K., 2002.

(5) Coughlan, C.; Ibanez, M.; Dobrozhan, O.; Singh, A.; Cabot, A.; Ryan, K. M. Compound copper chalcogenide nanocrystals. *Chem. Rev.* 2017, 117, 5865−6109.

(6) Reiss, P.; Carriere, M.; Lincheneau, C.; Vaure, L.; Tamang, S. Synthesis of semiconductor nanocrystals, focusing on nontoxic and earth-abundant materials. *Chem. Rev.* 2016, 116, 10731−10819.

(7) Khalate, S.; Kate, R.; Deokate, R. A review on energy economics and the recent research and development in energy and the Cu_2ZnSnS_4 (CZTS) solar cells: A focus towards efficiency. *Sol. Energy* 2018, 169, 616−633.

(8) Li, W.; Tan, J. M. R.; Leow, S. W.; Lie, S.; Magdassi, S.; Wong, L. H. Recent Progress in Solution-Processed Copper-Chalcogenide Thin-Film Solar Cells. *Energy Technol.* 2018, 6, 46−59.

(9) Vanalakar, S.; Agawane, G.; Shin, S.; Suryawanshi, M.; Gurav, K.; Jeon, K.; Patil, P.; Jeong, C.; Kim, J.; Kim, J. A review on pulsed laser deposited CZTS thin films for solar cell applications. *J. Alloys Compd.* 2015, 619, 109−121.

(10) Coughlan, C.; Ryan, K. M. Complete study of the composition and shape evolution in the synthesis of Cu_2ZnSnS_4 (CZTS) semiconductor nanocrystals. *CrystEngComm* 2015, 17, 6914−6922.

(11) Zhang, X.; Wu, X.; Centeno, A.; Ryan, M. P.; Alford, N. M.; Riley, D. J.; Xie, F. Significant broadband photocurrent enhancement by Au-CZTS core-shell nanostructured photocathodes. *Sci. Rep.* 2016, 6, No. 23364.

(12) Shavel, A.; Ibáñez, M.; Luo, Z.; De Roo, J.; Carrete, A.; Dimitrievska, M.; Genç, A.; Meyns, M.; Pe'rez-Rodrı'guez, A.; Kovalenko, M. V.; et al. Scalable heating-up synthesis of monodisperse Cu_2ZnSnS_4 nanocrystals. *Chem. Mater.* 2016, 28, 720−726.

(13) Ibáñez, M.; Berestok, T.; Dobrozhan, O.; LaLonde, A.; Izquierdo-Roca, V.; Shavel, A.; Pérez-Rodríguez, A.; Snyder, G. J.; Cabot, A. Phosphonic acids aid composition adjustment in the synthesis of $Cu_{2+x}Zn_{1-x}SnSe_{4-y}$ nanoparticles. *J. Nanopart. Res.* 2016, 18, No. 226.

(14) Li, Y.; Han, Q.; Kim, T. W.; Shi, W. Synthesis of wurtzite−zincblende Cu_2ZnSnS_4 and $Cu_2ZnSnSe_4$ nanocrystals: insight into the structural selection of quaternary and ternary compounds influenced by binary nuclei. *Nanoscale* 2014, 6, 3777−3785.

(15) Singh, S.; Liu, P.; Singh, A.; Coughlan, C.; Wang, J.; Lusi, M.; Ryan, K. M. Colloidal $Cu_2ZnSn(SSe)_4$ (CZTSSe) nanocrystals: shape and crystal phase control to form dots, arrows, ellipsoids, and rods. *Chem. Mater.* 2015, 27, 4742−4748.

(16) Gao, Y.; Wang, J.; Mo, S.; Wang, F.; Long, F.; Zou, Z. Synthesis of High-Quality Wurtzite $Cu_2ZnSn(S_{1-x}, Se_x)_4$ Nanocrystals With Non-Toxic Selenium Precursor and the Photoelectrochemical Performance of ZnO NAs/CZTSSe Heterojunction. *Sol. RRL* 2, 1800015. DOI: 10.1002/solr.201800015.

(17) Zheng, X.; Liu, Y.; Du, Y.; Sun, Y.; Li, J.; Zhang, R.; Li, Q.; Chen, P.; Zhao, G.; Fang, Y.; Dai, N. P-type quaternary chalcogenides of $Cu_2ZnSn(S, Se)_4$ nanocrystals: Large-scale synthesis, bandgap engineering and their thermoelectric performances. *J. Alloys Compd.* 2018, 738, 484−490.

(18) Jain, S.; Chawla, P.; Sharma, S. N.; Singh, D.; Vijayan, N. Efficient colloidal route to pure phase kesterite Cu_2ZnSnS_4 (CZTS) nanocrystals with controlled shape and structure. *Superlattices Microstuct.* 2018, 119, 59−71.

(19) Wang, J.-j.; Liu, P.; Seaton, C. C.; Ryan, K. M. Complete colloidal synthesis of Cu$_2$SnSe$_3$ nanocrystals with crystal phase and shape control. *J. Am. Chem. Soc.* **2014**, *136*, 7954−7960.

(20) Bag, S.; Gunawan, O.; Gokmen, T.; Zhu, Y.; Todorov, T. K.; Mitzi, D. B. Low band gap liquid-processed CZTSe solar cell with 10.1% efficiency. *Energy Environ. Sci.* **2012**, *5*, 7060−7065.

(21) Wang, W.; Winkler, M. T.; Gunawan, O.; Gokmen, T.; Todorov, T. K.; Zhu, Y.; Mitzi, D. B. Device characteristics of CZTSSe thin-film solar cells with 12.6% efficiency. *Adv. Energy Mater.* **2014**, *4*, No. 1301465.

(22) Hsu, W.-C.; Bob, B.; Yang, W.; Chung, C.-H.; Yang, Y. Reaction pathways for the formation of Cu$_2$ZnSn (Se, S)$_4$ absorber materials from liquid-phase hydrazine-based precursor inks. *Energy Environ. Sci.* **2012**, *5*, 8564−8571.

(23) Chen, S.; Gong, X.; Walsh, A.; Wei, S.-H. Crystal and electronic band structure of Cu$_2$ZnSnX$_4$ (X= S and Se) photovoltaic absorbers: First-principles insights. *Appl. Phys. Lett.* **2009**, *94*, No. 041903.

(24) Grossberg, M.; Krustok, J.; Timmo, K.; Altosaar, M. Radiative recombination in Cu$_2$ZnSnSe$_4$ monograins studied by photoluminescence spectroscopy. *Thin Solid Films* **2009**, *517*, 2489−2492.

(25) Ahn, S.; Jung, S.; Gwak, J.; Cho, A.; Shin, K.; Yoon, K.; Park, D.; Cheong, H.; Yun, J. H. Determination of band gap energy (Eg) of Cu$_2$ZnSnSe$_4$ thin films: on the discrepancies of reported band gap values. *Appl. Phys. Lett.* **2010**, *97*, No. 021905.

(26) Babu, G. S.; Kumar, Y. K.; Bhaskar, P. U.; Raja, V. S. Growth and characterization of co-evaporated Cu$_2$ZnSnSe$_4$ thin films for photovoltaic applications. *J. Phys. D: Appl. Phys.* **2008**, *41*, No. 205305.

(27) Todorov, T. K.; Reuter, K. B.; Mitzi, D. B. High-efficiency solar cell with earth-abundant liquid-processed absorber. *Adv. Mater.* **2010**, *22*, E156−E159.

(28) Chen, D.; Zhao, Y.; Chen, Y.; Wang, B.; Wang, Y.; Zhou, J.; Liang, Z. Hot-injection synthesis of Cu-doped Cu2ZnSnSe4 nanocrystals to reach thermoelectric zT of 0.70 at 450 C. *ACS Appl. Mater. Interfaces* **2015**, *7*, 24403−24408.

(29) Fan, F. J.; Wang, Y. X.; Liu, X. J.; Wu, L.; Yu, S. H. Large-Scale Colloidal Synthesis of Non-Stoichiometric Cu$_2$ZnSnSe$_4$ Nanocrystals for Thermoelectric Applications. *Adv. Mater.* **2012**, *24*, 6158−6163.

(30) van Embden, J.; Chesman, A. S. R.; Jasieniak, J. J. The Heat-Up Synthesis of Colloidal Nanocrystals. *Chem. Mater.* **2015**, *27*, 2246−2285.

(31) Smith, A. M.; Nie, S. Semiconductor nanocrystals: structure, properties, and band gap engineering. *Acc. Chem. Res.* **2010**, *43*, 190−200.

(32) Peng, X. Mechanisms for the shape-control and shape-evolution of colloidal semiconductor nanocrystals. *Adv. Mater.* **2003**, *15*, 459−463.

(33) Thanh, N. T.; Maclean, N.; Mahiddine, S. Mechanisms of nucleation and growth of nanoparticles in solution. *Chem. Rev.* **2014**, *114*, 7610−7630.

(34) Ryan, K. M.; Singh, S.; Liu, P.; Singh, A. Assembly of binary, ternary and quaternary compound semiconductor nanorods: From local to device scale ordering influenced by surface charge. *CrystEngComm* **2014**, *16*, 9446−9454.

(35) Singh, A.; Coughlan, C.; Milliron, D. J.; Ryan, K. M. Solution Synthesis and Assembly of Wurtzite-Derived Cu−In−Zn−S Nanorods with Tunable Composition and Band Gap. *Chem. Mater.* **2015**, *27*, 1517−1523.

(36) Wang, J.-J.; Liu, P.; Ryan, K. M. A facile phosphine-free colloidal synthesis of Cu$_2$SnS$_3$ and Cu$_2$ZnSnS$_4$ nanorods with a controllable aspect ratio. *Chem. Commun.* **2015**, *51*, 13810−13813.

(37) Singh, S.; Ryan, K. M. Occurrence of Polytypism in Compound Colloidal Metal Chalcogenide Nanocrystals, Opportunities, and Challenges. *J. Phys. Chem. Lett.* **2015**, *6*, 3141−3148.

(38) Lin, X.; Kavalakkatt, J.; Kornhuber, K.; Abou-Ras, D.; Schorr, S.; Lux-Steiner, M. C.; Ennaoui, A. Synthesis of Cu$_2$Zn$_x$Sn$_y$Se$_{1+x+2y}$ nanocrystals with wurtzite-derived structure. *RSC Adv.* **2012**, *2*, 9894−9898.

(39) Wang, J.-J.; Hu, J.-S.; Guo, Y.-G.; Wan, L.-J. Wurtzite Cu$_2$ZnSnSe$_4$ nanocrystals for high-performance organic−inorganic hybrid photodetectors. *NPG Asia Mater.* **2012**, *4*, No. e2.

(40) Kush, P.; Deka, S. Anisotropic kesterite Cu$_2$ZnSnSe$_4$ colloidal nanoparticles: Photoelectrical and photocatalytic properties. *Mater. Chem. Phys.* **2015**, *162*, 608−616.

(41) Wei, K.; Nolas, G. S. Synthesis and characterization of nanostructured stannite Cu$_2$ZnSnSe$_4$ and Ag$_2$ZnSnSe$_4$ for thermoelectric applications. *ACS Appl. Mater. Interfaces* **2015**, *7*, 9752−9757.

(42) Shavel, A.; Arbiol, J.; Cabot, A. Synthesis of Quaternary Chalcogenide Nanocrystals: Stannite Cu$_2$Zn$_x$Sn$_y$Se$_{1+x+2y}$. *J. Am. Chem. Soc.* **2010**, *132*, 4514−4515.

(43) Wei, H.; Guo, W.; Sun, Y.; Yang, Z.; Zhang, Y. Hot-injection synthesis and characterization of quaternary Cu$_2$ZnSnSe$_4$ nanocrystals. *Mater. Lett.* **2010**, *64*, 1424−1426.

(44) Park, C.; Cheong, B.-H.; Lee, K.-H.; Chang, K.-J. Structural and electronic properties of cubic, 2H, 4H, and 6H SiC. *Phys. Rev. B* **1994**, *49*, 4485.

(45) Yeh, C.-Y.; Lu, Z.; Froyen, S.; Zunger, A. Zinc-blende−wurtzite polytypism in semiconductors. *Phys. Rev. B* **1992**, *46*, 10086.

(46) Ito, T. Simple criterion for wurtzite-zinc-blende polytypism in semiconductors. *Jpn. J. Appl. Phys.* **1998**, *37*, L1217.

(47) Manna, L.; Milliron, D. J.; Meisel, A.; Scher, E. C.; Alivisatos, A. P. Controlled growth of tetrapod-branched inorganic nanocrystals. *Nat. Mater.* **2003**, *2*, 382.

(48) Manna, L.; Scher, E. C.; Alivisatos, A. P. Synthesis of soluble and processable rod-, arrow-, teardrop-, and tetrapod-shaped CdSe nanocrystals. *J. Am. Chem. Soc.* **2000**, *122*, 12700−12706.

(49) Kanaras, A. G.; Sönnichsen, C.; Liu, H.; Alivisatos, A. P. Controlled synthesis of hyperbranched inorganic nanocrystals with rich three-dimensional structures. *Nano Lett.* **2005**, *5*, 2164−2167.

(50) Milliron, D. J.; Hughes, S. M.; Cui, Y.; Manna, L.; Li, J.; Wang, L.-W.; Alivisatos, A. P. Colloidal nanocrystal heterostructures with linear and branched topology. *Nature* **2004**, *430*, 190.

(51) Chen, M.; Xie, Y.; Lu, J.; Xiong, Y.; Zhang, S.; Qian, Y.; Liu, X. Synthesis of rod-, twinrod-, and tetrapod-shaped CdS nanocrystals using a highly oriented solvothermal recrystallization technique. *J. Mater. Chem.* **2002**, *12*, 748−753.

(52) Jun, Y.-w.; Lee, S.-M.; Kang, N.-J.; Cheon, J. Controlled synthesis of multi-armed CdS nanorod architectures using monosurfactant system. *J. Am. Chem. Soc.* **2001**, *123*, 5150−5151.

(53) Talapin, D. V.; Nelson, J. H.; Shevchenko, E. V.; Aloni, S.; Sadtler, B.; Alivisatos, A. P. Seeded growth of highly luminescent CdSe/CdS nanoheterostructures with rod and tetrapod morphologies. *Nano Lett.* **2007**, *7*, 2951−2959.

(54) Choi, C. L.; Koski, K. J.; Sivasankar, S.; Alivisatos, A. P. Strain-dependent photoluminescence behavior of CdSe/CdS nanocrystals with spherical, linear, and branched topologies. *Nano Lett.* **2009**, *9*, 3544−3549.

(55) Cozzoli, P. D.; Manna, L.; Curri, M. L.; Kudera, S.; Giannini, C.; Striccoli, M.; Agostiano, A. Shape and phase control of colloidal ZnSe nanocrystals. *Chem. Mater.* **2005**, *17*, 1296−1306.

(56) Jiang, F.; Li, Y.; Ye, M.; Fan, L.; Ding, Y.; Li, Y. Ligand-tuned shape control, oriented assembly, and electrochemical characterization of colloidal ZnTe nanocrystals. *Chem. Mater.* **2010**, *22*, 4632−4641.

(57) Zamani, R. R.; Ibáñez, M.; Luysberg, M.; Garcia-Castello, N.; Houben, L.; Prades, J. D.; Grillo, V.; Dunin-Borkowski, R. E.; Morante, J. R.; Cabot, A.; Arbiol, J. Polarity-driven polytypic branching in Cu-based quaternary chalcogenide nanostructures. *ACS Nano* **2014**, *8*, 2290−2301.

(58) Wang, J.; Singh, A.; Liu, P.; Singh, S.; Coughlan, C.; Guo, Y.; Ryan, K. M. Colloidal synthesis of Cu$_2$SnSe$_3$ tetrapod nanocrystals. *J. Am. Chem. Soc.* **2013**, *135*, 7835−7838.

(59) Miszta, K.; De Graaf, J.; Bertoni, G.; Dorfs, D.; Brescia, R.; Marras, S.; Ceseracciu, L.; Cingolani, R.; Van Roij, R.; Dijkstra, M.; Manna, L. Hierarchical self-assembly of suspended branched colloidal nanocrystals into superlattice structures. *Nat. Mater.* **2011**, *10*, 872.

(60) Qi, W.; Graaf, Jd.; Qiao, F.; Marras, S.; Manna, L.; Dijkstra, M. Ordered two-dimensional superstructures of colloidal octapod-shaped nanocrystals on flat substrates. *Nano Lett.* **2012**, *12*, 5299−5303.

(61) Li, H.; Kanaras, A. G.; Manna, L. Colloidal branched semiconductor nanocrystals: state of the art and perspectives. *Acc. Chem. Res.* **2013**, *46*, 1387−1396.

(62) Sun, B.; Marx, E.; Greenham, N. C. Photovoltaic devices using blends of branched CdSe nanoparticles and conjugated polymers. *Nano Lett.* **2003**, *3*, 961−963.

(63) Dayal, S.; Zhong, H.; Kopidakis, N.; Scholes, G. D.; Rumbles, G. Improved power conversion efficiency for bulk heterojunction solar cells incorporating CdTe-CdSe nanoheterostructure acceptors and a conjugated polymer donor. *J. Photon. Energy* **2015**, *5*, No. 057409.

(64) Mishra, N.; Mukherjee, B.; Xing, G.; Chakrabortty, S.; Guchhait, A.; Lim, J. Cation exchange synthesis of uniform PbSe/PbS core/shell tetra-pods and their use as near-infrared photodetectors. *Nanoscale* **2016**, *8*, 14203−14212.

(65) Zebarjadi, M.; Esfarjani, K.; Dresselhaus, M.; Ren, Z.; Chen, G. Perspectives on thermoelectrics: from fundamentals to device applications. *Energy Environ. Sci.* **2012**, *5*, 5147−5162.

(66) Soni, A.; Shen, Y.; Yin, M.; Zhao, Y.; Yu, L.; Hu, X.; Dong, Z.; Khor, K. A.; Dresselhaus, M. S.; Xiong, Q. Interface driven energy filtering of thermoelectric power in spark plasma sintered $Bi_2Te_{2.7}Se_{0.3}$ nanoplatelet composites. *Nano Lett.* **2012**, *12*, 4305−4310.

(67) Szczech, J. R.; Higgins, J. M.; Jin, S. Enhancement of the thermoelectric properties in nanoscale and nanostructured materials. *J. Mater. Chem.* **2011**, *21*, 4037−4055.

(68) Wu, L.; Fan, F.-J.; Gong, M.; Ge, J.; Yu, S.-H. Selective epitaxial growth of zinc blende-derivative on wurtzite-derivative: the case of polytypic $Cu_2CdSn(S_{1-x}Se_x)_4$ nanocrystals. *Nanoscale* **2014**, *6*, 3418−3422.

(69) Ananthakumar, S.; Kumar, J. R.; Babu, S. M. Synthesis of $Cu_2ZnSnSe_4$ hierarchical nanostructures by colloidal method. *Optik* **2016**, *127*, 10360−10365.

(70) Uccelli, E.; Arbiol, J.; Magen, C.; Krogstrup, P.; Russo-Averchi, E.; Heiss, M.; Mugny, G.; Morier-Genoud, F.; Nygård, J.; Morante, J. R.; Morral, A. F. Three-dimensional multiple-order twinning of self-catalyzed GaAs nanowires on Si substrates. *Nano Lett.* **2011**, *11*, 3827−3832.

(71) Utama, M. I. B.; de la Mata, M.; Magen, C.; Arbiol, J.; Xiong, Q. Twinning-, Polytypism-, and Polarity-Induced Morphological Modulation in Nonplanar Nanostructures with van der Waals Epitaxy. *Adv. Funct. Mater.* **2013**, *23*, 1636−1646.

(72) Peng, Z. A.; Peng, X. Mechanisms of the shape evolution of CdSe nanocrystals. *J. Am. Chem. Soc.* **2001**, *123*, 1389−1395.

(73) Orbaek, A. W.; Morrow, L.; Maguire-Boyle, S. J.; Barron, A. R. Reagent control over the composition of mixed metal oxide nanoparticles. *J. Exp. Nanosci.* **2015**, *10*, 324−349.

(74) Irkhina, A.; Levcenko, S.; Hinrichs, V.; Plate, P.; Unold, T. Metal acetate based synthesis of small-sized Cu_2ZnSnS_4 nanocrystals: effect of injection temperature and synthesis time. *RSC Adv.* **2017**, *7*, 11752−11760.

(75) Yin, X.; Shi, M.; Wu, J.; Pan, Y.-T.; Gray, D. L.; Bertke, J. A.; Yang, H. Quantitative analysis of different formation modes of platinum nanocrystals controlled by ligand chemistry. *Nano Lett.* **2017**, *17*, 6146−6150.

(76) Kar, M.; Agrawal, R.; Hillhouse, H. W. Formation pathway of $CuInSe_2$ nanocrystals for solar cells. *J. Am. Chem. Soc.* **2011**, *133*, 17239−17247.

(77) Grisaru, H.; Palchik, O.; Gedanken, A.; Palchik, V.; Slifkin, M. A.; Weiss, A. M. Microwave-assisted polyol synthesis of $CuInTe_2$ and $CuInSe_2$ nanoparticles. *Inorg. Chem.* **2003**, *42*, 7148−7155.

(78) Chun, Y.-G.; Kim, K.-H.; Yoon, K.-H. Synthesis of $CuInGaSe_2$ nanoparticles by solvothermal route. *Thin Solid Films* **2005**, *480*, 46−49.

(79) Yin, D.; Liu, Y.; Dun, C.; Carroll, D. L.; Swihart, M. T. Controllable colloidal synthesis of anisotropic tin dichalcogenide

nanocrystals for thin film thermoelectrics. *Nanoscale* **2018**, *10*, 2533−2541.

(80) Wang, J.-J.; Ryan, K. M. Colloidal synthesis of Cu_2SnSe_3 nanocrystals with structure induced shape evolution. *CrystEngComm* **2016**, *18*, 3161−3169.

(81) Zhai, X.; Jia, H.; Zhang, Y.; Lei, Y.; Wei, J.; Gao, Y.; Chu, J.; He, W.; Yin, J.-J.; Zheng, Z. In situ fabrication of Cu_2ZnSnS_4 nanoflake thin films on both rigid and flexible substrates. *CrystEngComm* **2014**, *16*, 6244.

(82) Altosaar, M.; Raudoja, J.; Timmo, K.; Danilson, M.; Grossberg, M.; Krustok, J.; Mellikov, E. $Cu_2Zn_{1-x}Cd_xSn(Se_{1-y}S_y)_4$ solid solutions as absorber materials for solar cells. *Phys. Status Solidi (a)* **2008**, *205*, 167−170.

(83) Lucas, F. W. dS.; Lima, A. R. F.; Mascaro, L. H. Glycerol as additive in copper indium gallium diselenide electrodeposition: morphological, structural and electronic effects. *RSC Adv.* **2015**, *5*, 18295−18300.

(84) Gonzalez, J. M.; Oleynik, I. I. Layer-dependent properties of SnS_2 and $SnSe_2$ novel two-dimensional materials. *Phys. Rev. B* **2016**, *94*, No. 125443.

(85) De Trizio, L.; Li, H.; Casu, A.; Genovese, A.; Sathya, A.; Messina, G. C.; Manna, L. Sn cation valency dependence in cation exchange reactions involving $Cu_{(2-x)}Se$ nanocrystals. *J. Am. Chem. Soc.* **2014**, *136*, 16277−16284.

(86) Pinto, A. H.; Leite, E. R.; Longo, E.; de Camargo, E. R. Crystallization at room temperature from amorphous to trigonal selenium as a byproduct of the synthesis of water dispersible zinc selenide. *Mater. Lett.* **2012**, *87*, 62−65.

(87) Wang, J.; Singh, A.; Liu, P.; Singh, S.; Coughlan, C.; Guo, Y.; Ryan, K. M. Colloidal synthesis of Cu_2SnSe_3 tetrapod nanocrystals. *J. Am. Chem. Soc.* **2013**, *135*, 7835−7838.

(88) Ostwald, W. Wilhelm Ostwald-Studien über die Bildung und Umwandlung fester Körper. *Z. Phys. Chem.* **1897**, *22*, 289−330.

(89) Sahu, P.; Prasad, B. L. Time and temperature effects on the digestive ripening of gold nanoparticles: is there a crossover from digestive ripening to Ostwald ripening? *Langmuir* **2014**, *30*, 10143−10150.

(90) Bastús, N. G.; Comenge, J.; Puntes, V. Kinetically controlled seeded growth synthesis of citrate-stabilized gold nanoparticles of up to 200 nm: size focusing versus Ostwald ripening. *Langmuir* **2011**, *27*, 11098−11105.

(91) Howard, A.; Mitchell, C.; Egdell, R. Real time STM observation of Ostwald ripening of Pd nanoparticles on TiO_2 (1 1 0) at elevated temperature. *Surf. Sci.* **2002**, *515*, L504−L508.

(92) Brutchey, R. L. Diorganyl dichalcogenides as useful synthons for colloidal semiconductor nanocrystals. *Acc. Chem. Res.* **2015**, *48*, 2918−2926.